The International Journal of Advanced Manufacturing Technology (2025) 140:6483–6503
https://doi.org/10.1007/s00170-025-16597-2

ORIGINAL ARTICLE

Experimental data–driven framework for quality control of 3D-printed concrete permanent formworks

Tae-Kyung Kim[1] · Sangwoo Oh[2] · Jinsuk Lee[1] · Seongcheol Choi[2] · Chang-Su Shim[2]

Received: 14 July 2025 / Accepted: 12 September 2025 / Published online: 7 October 2025
© The Author(s) 2025

Abstract
As an emerging structural system, 3D-printed concrete permanent formwork (3DPF) eliminates the need for formwork removal and enables the realization of complex geometries. However, clearly defined quality control standards tailored to the unique characteristics of 3DPF are still lacking. The novelty of this study lies in developing an experimental data–based framework to integrate quality control considerations into both the design and manufacturing stages. The proposed framework comprises systematic experimental procedures to evaluate parameters such as the fresh and hardened material properties, printing parameters, and geometric constraints and organizes the results into structured data categories. The collected data were subsequently embedded into a design for additive manufacturing (DfAM) decision-making algorithm, which supports manufacturability evaluations, including additional layers for milling, plastic collapse prediction, maximum printable dimensions, and first-layer deformation near sharp corners. An equivalent strength factor was introduced as a quality control reference during printing, providing a consistent basis for evaluating structural performance using the strength ratio between the printed and cast specimens. Moreover, an exponential relationship was identified between the corner angle and first layer width, enabling the quantification of layer deformation near sharp corners. Finally, the proposed framework enables unified quality control across the materials, equipment, and design of the 3DPF and its manufacturing system.

Keywords 3D concrete printing · 3D-printed concrete permanent formwork · Design for additive manufacturing · Quality control

1 Introduction

The technology of 3D printing has had a significant impact on various industries, including the healthcare, aerospace, and automotive sectors. Recently, 3D concrete printing (3DCP), which uses cementitious materials, has gained momentum in the construction industry [1–4]. One key application of this technology is 3D-printed concrete permanent formwork (3DPF), which offers a viable method for producing geometrically complex geometries that are difficult to achieve using conventional construction methods [5, 6]. This technological advantage enables the realization of infrastructure that satisfies both aesthetic and structural performance requirements. Additionally, 3DPF allows the direct printing of concrete formwork that remains permanently integrated into the structural element, eliminating the need for assembly and removal associated with traditional formwork. However, standards and quality control guidelines for ensuring the reliable quality of 3DPF have yet to be established. Therefore, a systematic approach is required to ensure quality control by considering the unique characteristics of 3DCP and incorporating them effectively into the design and manufacturing stages.

In 3DCP, a layer-by-layer deposition process using cementitious materials is employed, resulting in structural and constructional characteristics that are different from those of traditional cast-in-place (CIP) concrete. A 3DPF manufactured using this method will inherently contain interlayer interfaces that influence its anisotropic structural responses [7–9]. Despite these unique characteristics, current quality control guidelines are primarily based on CIP

✉ Chang-Su Shim
csshim@cau.ac.kr

[1] Department of Smart Cities, Chung-Ang University, 84 Heukseok-ro, Dongjak-gu, Seoul 06974, Republic of Korea

[2] Department of Civil and Environmental Engineering, Urban Design and Studies, Chung-Ang University, 84 Heukseok-Ro, Dongjak-Gu, Seoul 06974, Republic of Korea

concrete, rendering them inadequate for the specific manufacturing process of 3DPF.

Previous studies have primarily focused on evaluating material properties and printing stability. For instance, inline sensor–based evaluations have been proposed to assess extrudability [10, 11], and buildability prediction models based on the rheological properties of materials have been developed [12, 13]. Due to the layered nature of additive manufacturing, interlayer interfaces are inevitable, leading to anisotropic structural behavior. Accordingly, several studies have analyzed this anisotropy and explored strategies to mitigate it [14, 15]. In addition, the geometric quality of the extruded material without formwork has been investigated through simulations, and post-processing methods such as milling have been introduced to improve dimensional accuracy and surface quality [16, 17]. However, to ensure that these evaluation methods ultimately lead to high-quality 3DPF manufacturing, a methodology that directly incorporates the performance indicators of 3DCP and 3DPF into the design stage must be established. This highlights the need for a quality control framework that integrates the materials, equipment, and design into a single manufacturing system.

The DfAM approach has attracted attention as a strategy for achieving integrated quality control [18]. The DfAM methodology incorporates the constraints of additive manufacturing during the design stage to prevent fabrication failures and errors. The design model of a printed object can embed information on material characteristics, printing parameters, and post-processing requirements [19, 20]. Previous studies have proposed building information modeling (BIM)-based automatic path generation [21–23], the definition of digital engineering models for 3DPF members [24], and optimization techniques for the design of structures fabricated using 3DCP [25, 26]. These efforts highlight the potential of DfAM-based design methodologies for 3DCP. However, because these approaches focus primarily on design information, integrating them with key quality control data from actual fabrication systems will further enhance their applicability and robustness.

This study developed a 3DPF fabrication system based on the construction process proposed by Kim et al. [24]. The proposed system extends beyond simple printing to include rebar and duct placement, concrete casting, and robot-assisted milling for surface finishing to enable precise assembly between segments (Fig. 1). This process serves as a digital alternative to the conventional match-casting method, which typically requires high-precision molds and labor-intensive manual work to assemble precast segments. Accordingly, this study extracted experimental data for quality control based on the key fabrication steps of 3DPF and developed a DfAM-integrated strategy to incorporate these data into the early design stage.

2 Research objective and framework overview

The specific objective of this study was to develop an experimental data–driven framework to ensure the quality of 3DPF. The proposed framework consists of three key components: (1) an experimental program for acquiring data on fresh and hardened material properties and geometric constraints, and integrating material and printing parameters into a unified manufacturing system; (2) the collection of critical experimental data to support quality control in the manufacturing system; (3) the application of the collected data through a decision-making algorithm for DfAM, which connects experimental insights to the design stage as a comprehensive framework for 3DPF development. Previous studies mainly advanced or optimized individual aspects such as material properties, printing parameters, or design strategies. In contrast, this study defines

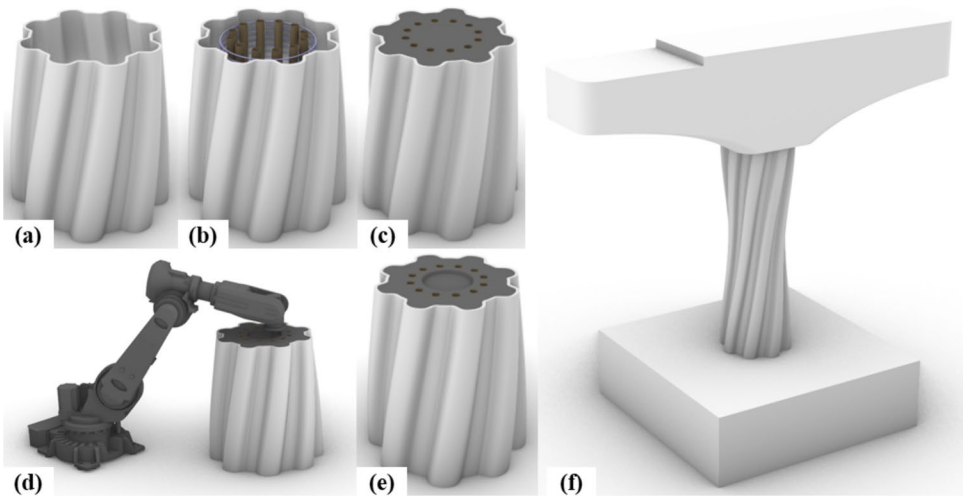


Fig. 1 Digital manufacturing process for prefabricated bridge pier: **a** 3DCP of segment permanent formwork; **b** placement of rebars and ducts; **c** casting of concrete within formwork; **d** milling joint surfaces of segments; **e** complete segments; **f** assembly of segments

an integrated manufacturing system for 3DPF by linking materials, process, and design considerations into a framework. If the individual contributions achieved in previous studies are integrated and applied within the framework proposed in this study, 3D concrete printing technology could advance to a more sophisticated stage.

To address the absence of a systematic quality control system for 3DPF, the framework was designed as an integrated approach in which material, equipment, and design are inherently linked. It includes the selection of appropriate printing parameters tailored to the material properties, evaluation of layer deformation, mechanical performance of printed material, and design modifications to accommodate surface finishing requirements and geometrical constraints. The overall structure of the proposed framework, including experimental data acquisition, structured data collection, and its application to the DfAM, is presented in Fig. 2. Each component is described in detail in the subsequent sections.

3 Experimental program for data acquisition

3.1 Test material

While conventional mix design concepts focus on performance parameters such as strength and durability, 3DCP materials must satisfy performance factors associated with printing and layer-by-layer deposition [27]. These factors include pumpability, extrudability, buildability, and opening time [28]. To ensure smooth flow from the mixer to the nozzle through the pipe and sustain the weight of the subsequently deposited layers during printing, 3DCP materials should exhibit highly thixotropic behavior, enabling rapid reversible structural build-up. Additionally, they should exhibit excellent shape retention with almost zero slump [29]. Delaying the irreversible structural build-up (cement hydration) is preferred to maintain material performance throughout the construction process.

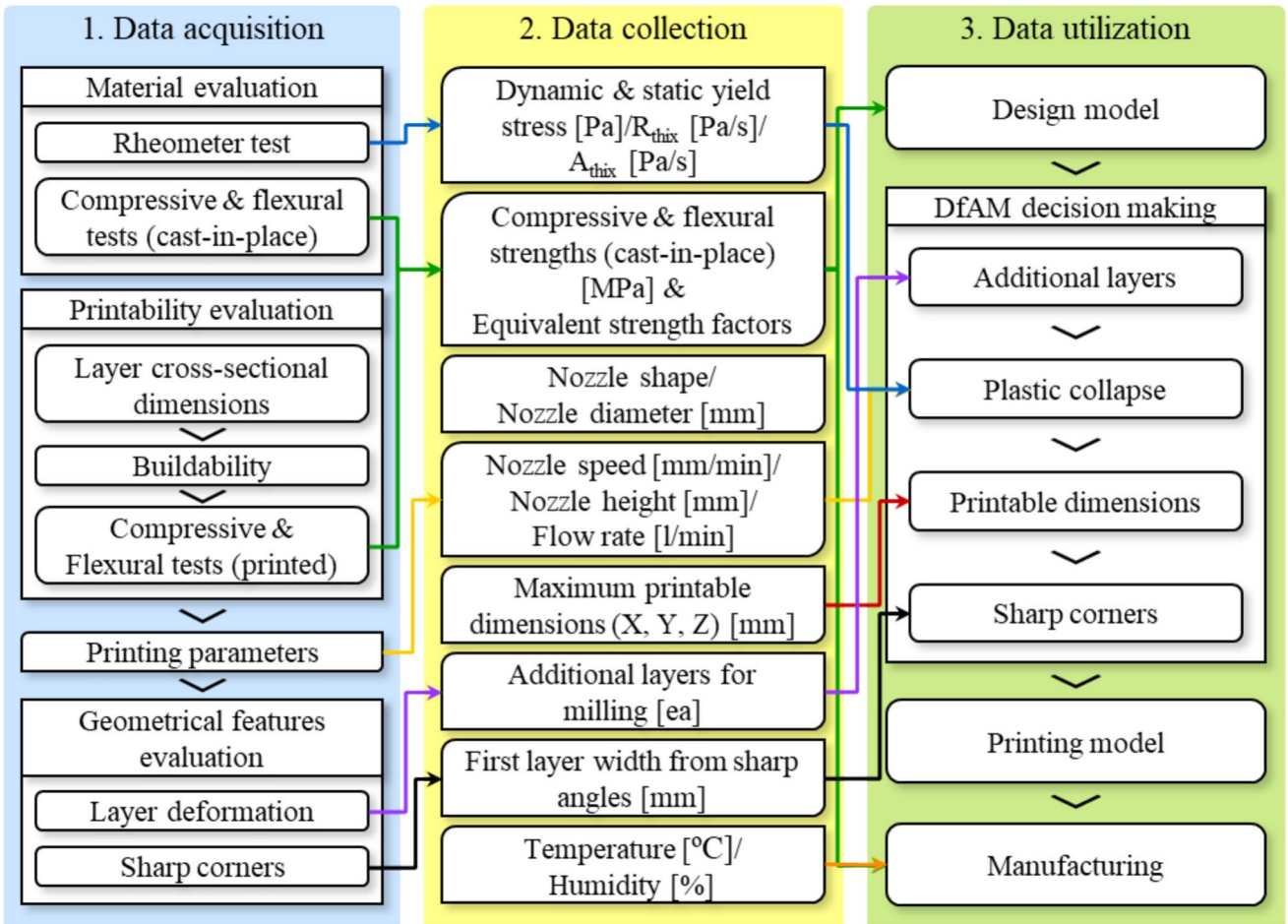


Fig. 2 Proposed framework sequence and data flow: systematic experimental data acquisition, structured data collection, and utilization in DfAM decision-making processes for 3DPF quality management

In this study, a low water-binder ratio was mostly used for the printing material, and admixtures such as high-water reducing agents (HWRA), viscosity-modifying agents (VMA), clay, and retarders were used in the mix design to achieve high-thixotropy materials to enhance flocculation [30–33]. The mixture used in this study was designed to achieve a high-strength composition using cement mortar with a low water-binder ratio. Ordinary Portland cement (Type I, KS L 5201 [34]) and fly ash (Type II, KS L 5405 [35]) were sourced from local suppliers. Their Blaine fineness and density were 349.9 m^2/kg and 3130 kg/m^3 for the cement and 404.0 m^2/kg and 2280 kg/m^3 for the fly ash, respectively. Silica fume was Microsilica® 940U (Elkem). The binder mass ratio of cement to fly ash to silica fume was 7:2:1, and the water-binder ratio was 0.30. The mortar used feldspar as the fine aggregate, with an aggregate-binder mass ratio of 55:45. A HWRA (polycarboxylate-ether based) and a VMA (cellulose-ether based) were used at 1.0% and 0.2% of the binder mass, respectively. The addition of HWRA enabled smooth transportation while simultaneously delaying cement hydration. Additionally, VMA was included in the mixture to resist material segregation during shearing caused by the pump. The binder composition, water-binder ratio, binder-aggregate ratio, and admixture dosage were adjusted through a trial-and-error method to align with the specifications of the 3D printer and the desired geometry of the target structure. Therefore, based on the mini-slump flow tests conducted in accordance with ASTM C1437 [36], the slump of the mixture was zero.

To prepare strength specimens, processing had to be uniform on all sides. Because processing tiny specimens after the material has completely hardened is difficult, the specimens were printed and cut after the initial setting time. The initial and final setting times of the material were measured according to ASTM C403 [37], with an initial setting time of 720 min and a final setting time of 1002 min.

3.2 Printing equipment and environmental conditions

Figure 3 shows the printing equipment used in this study. A three-axis 3D concrete printer with a round nozzle (diameter of 22 mm) was used. The maximum movement length of the printer was 1000 mm per axis. The material was uniformly mixed in a mixer, transferred to a pump, and extruded through a nozzle using a concrete vibrator to remove the voids in the layers. The total path length for the materials travelling from the mixer to the nozzle tip was 6.4 m. All experiments were conducted indoors, where the average temperature and relative humidity were 15.2 ± 1 °C and 61 ± 1%, respectively.

3.3 Material evaluation

3.3.1 Rheometer test

Rheology, the science of material deformation and flow, has recently been employed in concrete research to characterize and analyze the behavior of fresh mixtures in a quantitative and systematic manner [32, 38]. Kruger et al. [12] proposed a plastic yield prediction model based on rheological features for the evaluation of printing materials. In their method, a constant shear-rate test was conducted using a rheometer. Therefore, the rheology test was conducted at a shear rate of 1 s^{-1} (vane rate of 0.167 rev/s) following the same constant shear rate protocol used in the reference study. The torque measured during the test was converted into the shear stress using Eq. (1) [39]. The peak value was defined as the static yield stress, whereas the plateau value observed after the peak was considered the dynamic yield stress. The time-dependent evolution of the yield stress was analyzed using the equations proposed by Kruger et al. [12]. When reversible flocculation is the dominant mechanism, the rate of change is quantified as the re-flocculation rate (R_{thix}). In

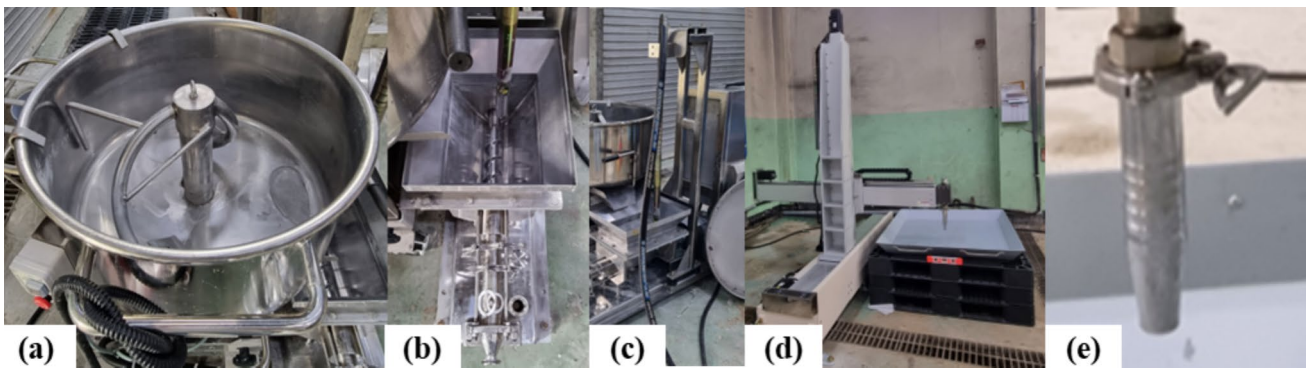


Fig. 3 Printer components: **a** mixer; **b** pump; **c** concrete vibrator; **d** three-axis gantry; **e** round nozzle with a diameter of 22 mm

contrast, when irreversible structuration caused by hydration prevails, the rate is defined as the structuration rate (A_{thix}).

$$\tau(t) = \frac{2T(t)}{\pi D^3(\frac{h}{D} + \frac{1}{3})} \quad (1)$$

where $\tau(t)$ is the shear stress (Pa) with time, t (min); $T(t)$ is the measured torque (Nm) with time, t (min); D and h are the diameter and height of the vane (m), respectively.

3.3.2 Compressive and flexural strengths of the CIP specimen

The compressive and flexural strengths of the printing materials were tested in accordance with the ASTM C109 [40] and ASTM C348 [41] standards (Fig. 4). Compressive strength specimens were prepared as 50 mm × 50 mm × 50 mm cubes, while the flexural strength specimens measured 40 mm × 40 mm × 160 mm. The standards employed in this subsection and Sect. 3.4.3. were selected based on the requirements of the specimen dimensions that could be produced within the layer width using 3D concrete printers. Each strength value was determined using the mean values derived from three specimens. Because the comparison was made against printed materials, the specimens were cured for 7 days in a chamber with constant temperature and humidity (temperature 22 ± 3 °C, relative humidity 50%) before being used in the strength tests.

There is no standardized methodology for evaluating the material strength of printed elements. The process of printing and cutting to produce a specimen is highly inefficient in terms of construction efficiency. The proposed framework compares the strengths of specimens fabricated through the CIP and printing methods using the material and proposed equivalent strengths to manage the quality of the printing process [42]. The equivalent strength can be expressed using Eqs. 2 and 3. In these equations, $f_{cm,3D}$ and $f_{rm,3D}$ are the mean compressive and flexural strengths of the printed materials, respectively; $f_{cm,CIP}$ and $f_{rm,CIP}$ are the mean compressive and flexural strengths of the CIP material, respectively; α and β are the equivalent strength ratios of the compressive and flexural strength, respectively.

$$f_{cm,3D} = \alpha \times f_{cm,\,cast} \quad (2)$$

$$f_{rm,3D} = \beta \times f_{rm,\,cast} \quad (3)$$

3.4 Printability evaluation

In the printability evaluation, the objective is to select printing parameters that are appropriate for the material and quantify the data obtained during the evaluation process for application in DfAM. The printing parameters significantly influence the material [43]. Moreover, the selection of printing parameters is essential for quality control in 3DCP [44, 45]. Consequently, the material and printing parameters should be considered in a unified manufacturing system to evaluate printability. In 3DCP, successful operation requires three key parameters: the nozzle speed (determines the velocity at which the nozzle traverses the print path), nozzle height (determines the thickness of each layer), and flow rate (controls the volume of the extruded material). Figure 5 illustrates these three printing parameters. The nozzle speed is in mm/min, the nozzle height is in mm, and the

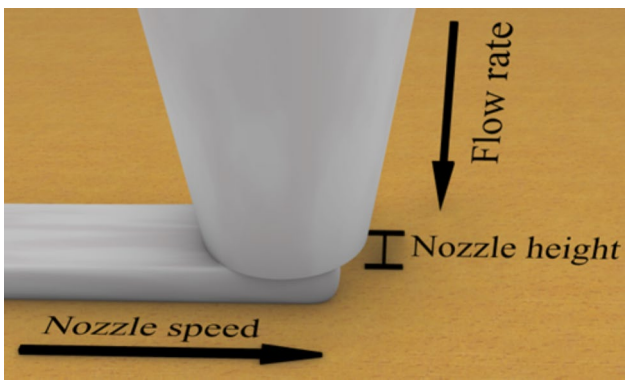


Fig. 5 Printing parameters used in printability evaluation

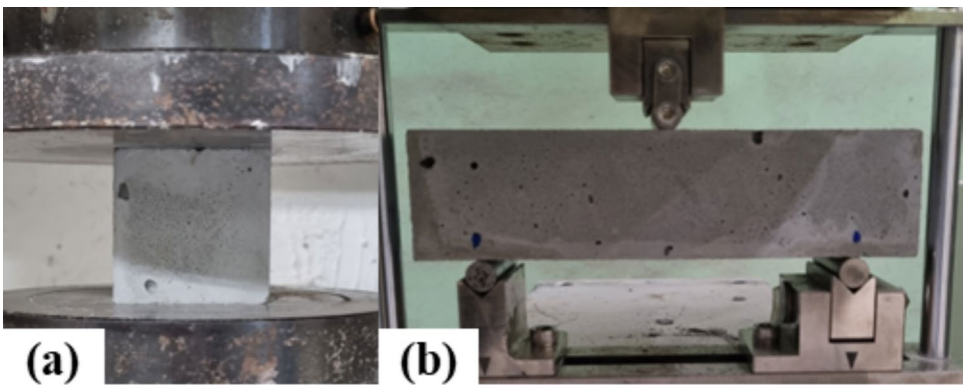


Fig. 4 Test setups for cast specimens: **a** compressive test in accordance with ASTM C109; **b** flexural test in accordance with ASTM C348

flow rate is in l/min. Depending on the development of the manufacturing system, additional printing parameters, such as the nozzle tip design or featured dimensions of screws, may also be present. However, this study focused only on basic printing parameters. The printability evaluation comprised the layer cross-sectional dimensions, buildability, and compressive and flexural strengths.

When a practitioner is first provided with materials and printing equipment, identifying appropriate printing parameters can be challenging. Therefore, a visual inspection of layer quality during preliminary prints is essential to determine the parameters best suited to the material. The range of printing parameters considered in the printability evaluation was narrowed before fully implementing the proposed framework. As shown in Fig. 6, if the nozzle height was too great, the material failed to be extruded at the intended location. If the layer width failed to satisfy the dimensional requirements for the planned strength specimens, the printing parameters were excluded.



Fig. 6 Visual inspection of layer quality in preliminary printing: **a** unstable extrusion caused by large nozzle height; **b** layer thickness insufficient for producing strength specimens

3.4.1 Layer cross-sectional dimensions

The cross-sectional dimensions of the extruded layers varied based on the material's rheological properties, nozzle height, nozzle speed, and flow rate. Measuring these dimensions provides a means to evaluate the material's buildability [46, 47]. Two key geometric indicators were considered: the effective width, which refers to the contact length with the subsequent layer, and the cross-sectional area, which reflects the self-weight imposed on the underlying layer and is defined as the area of the vertical section of a single layer.

As shown in Fig. 7, 400-mm-long straight layers were sequentially printed using the G-code, each with different printing parameters. After the final setting time of curing, the layers were cut and photographed for image-based measurements using ImageJ [48]. The effective width was measured as the maximum length along the upper surface that contacted the next layer, and the cross-sectional area was obtained by calculating the entire cross-sectional area. Based on the mean values of these two dimensions, the printing parameters that resulted in a larger effective width and smaller cross-sectional area were selected for subsequent evaluation.

3.4.2 Buildability

The printing parameters selected through the evaluation of layer cross-sectional dimensions were subsequently used to assess buildability. As the number of printed layers increases, the accumulated self-weight exceeds the yield

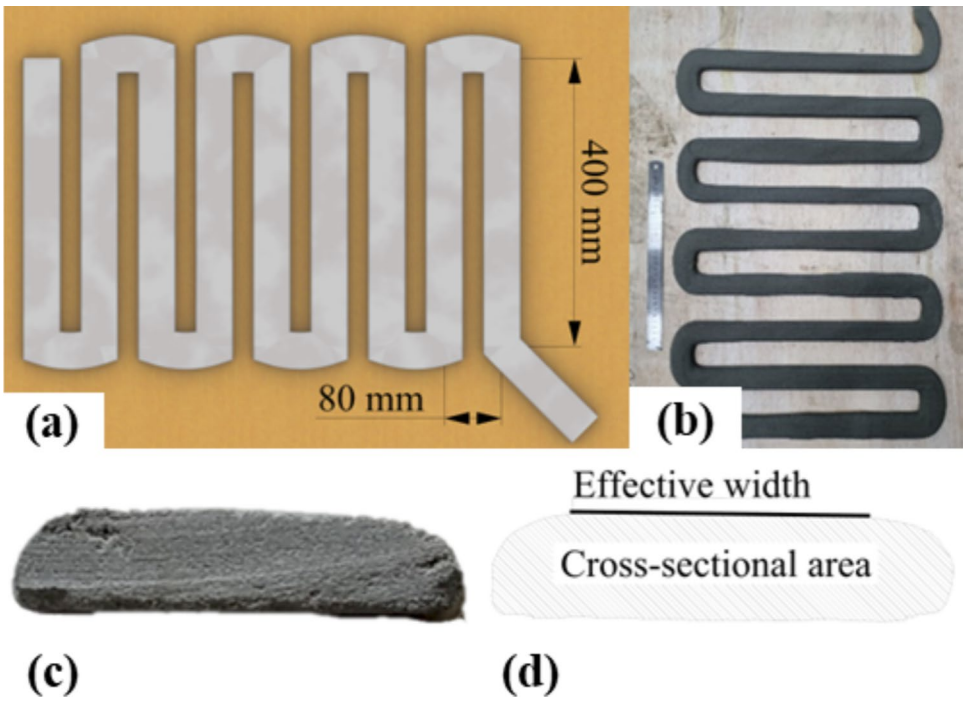


Fig. 7 Layer cross-sectional dimensions test: **a** single-layer printing model; **b** actual printed layer; **c** cross-section of cut layer; **d** cross-sectional dimensions of defined layer

stress of the bottom layer, resulting in loss of stability and eventual failure because of plastic buckling. To evaluate the buildability associated with the printing parameters, the single-strip printing model (length of 400 mm, reflecting the designated nozzle height) was employed. Buildability was quantified as the maximum number of layers printed before collapse. However, because a simplified model was used in this buildability evaluation, the results were not directly applied to the DfAM-driven design processes.

3.4.3 Compressive and flexural strength of printed specimen

The two printing parameters that achieved the best performance in the buildability assessment were selected and applied to the subsequent material strength evaluations. Printing parameters that resulted in lower strengths were excluded from the structural design of permanent formworks. Additionally, the experimental procedure described in Sect. 3.3.2 was carried out to evaluate the strength in all layer orientations, as shown in Fig. 8, and determine the equivalent strength with consideration to the material's anisotropy. As illustrated in Fig. 9a, a rectangular element with a side length of 400 mm, height of 180 mm, and corner radius of 25 mm was printed. After the initial setting time, to allow precise cutting, the printed element was trimmed to the required specimen dimensions using a bandsaw, as shown in Fig. 9b, and then cured for 7 days in a chamber under the same constant temperature and humidity conditions as the cast specimens. Subsequently, the strength in all printing directions was assessed using the test setup shown in Fig. 9c.

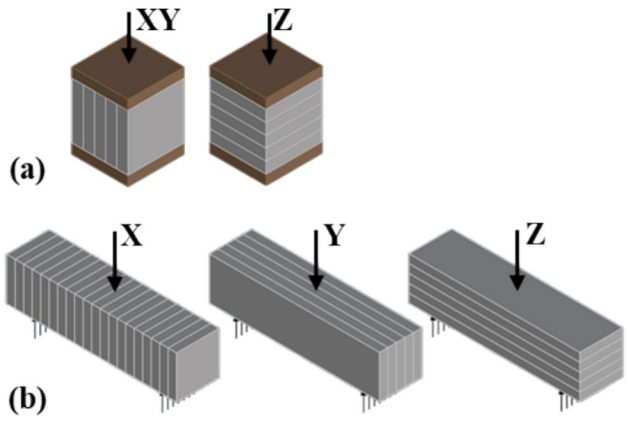


Fig. 8 Specimen orientations used to evaluate anisotropy in printed layers: **a** compressive strength specimens; **b** flexural strength specimens

3.5 Geometrical feature evaluation

Once the printing parameters are determined through printability evaluation, a 3DPF design that the manufacturing system can produce without defect failures must be quantified and managed in parallel. Although printability evaluation provides data on the rheological properties and mechanical strength of the material, the feasibility of realizing freeform geometries must also be considered to fully leverage the advantages of 3DPF. This approach strengthens both the DfAM and quality control for 3DPF. In the evaluation of geometrical features, layer deformation and sharp corners are assessed using the proposed experimental methods, and the results are systematically managed within the proposed framework.

3.5.1 Layer deformation

The quantification of layer deformation is a critical consideration for achieving the surface finishing of each segment in the digital manufacturing process of 3DPF members, as illustrated in Fig. 1. Owing to gravity and the self-weight of the deposited material, deformation can lead to printed formwork with a height lower than the target height specified in the design model. This discrepancy results in geometrical errors in the overall member. Therefore, to incorporate the required number of additional layers into the design during actual production, it is essential to obtain preliminary data that comprehensively reflect both the material deformation and intended cutting height. To this end, an experiment was conducted to evaluate layer deformation. Figure 10 presents the printed model comprising ten 400-mm-long layers, the actual printed structure, and its cross-section. In the cross-section, the width, thickness, and total height of the individual layers were measured to analyze the deformation extent.

3.5.2 Sharp corners

When 3D concrete printing complex geometries are used, the nozzle tends to dwell longer in the sharp corner regions, resulting in the material flow rate deviating from the intended value. This can lead to material waste, cracking caused by tensile stress at the outer corner [49], and potential interference between the 3DPF and reinforcement details. Therefore, to manage a feasible corner angle for implementing more complex geometries, a benchmark structure-printing model is proposed, as shown in Fig. 11. Considering the expected height difference between the inner and outer sides of the corner, the height discrepancy resulting from the inner and outer overfill was measured along with the width

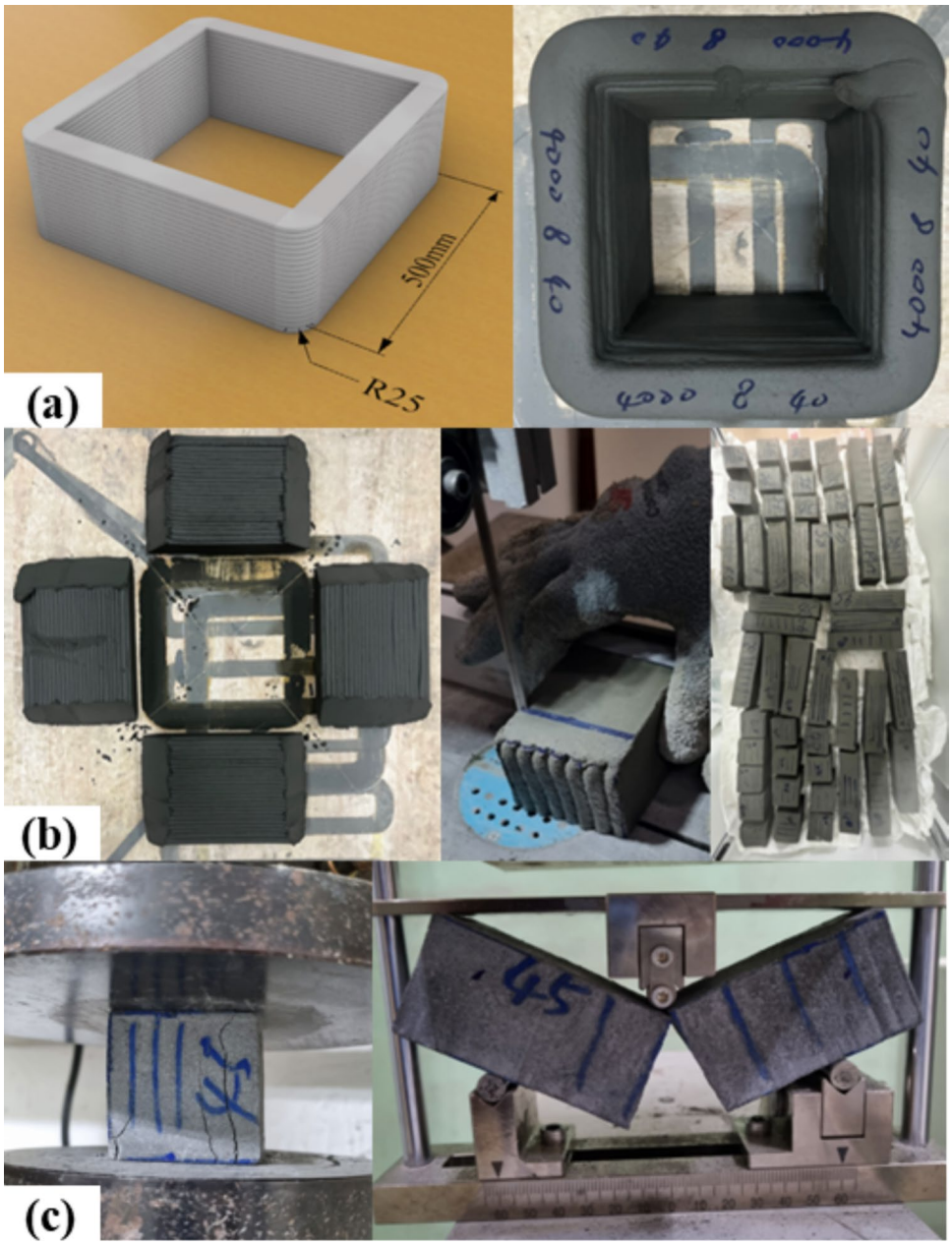


Fig. 9 Procedure for evaluating strength of printed materials: **a** printing model used for evaluation and actual printed structure; **b** specimens after cutting and curing; **c** test setups for measuring compressive and flexural strength of printed materials

of the first layer and compared with the layer deformation data presented in Sect. 3.5.1.

4 Experimental results

4.1 Rheological properties

The rheological properties of the printing material were measured to serve as reference data for assessing material quality and predicting buildability. The measured values are the dynamic yield shear stress of 1356.1 Pa, re-flocculation rate (R_{thix}) of 12.3 Pa/s, initial static yield shear stress of 2832.1 Pa, and structuration rate (A_{thix}) of 1.3 Pa/s, which indicate a high degree of thixotropy and progressive structuration, consistent with buildability requirements. These rheological measurements serve as reference data for practitioners to evaluate material quality by comparing batch-specific test results. Furthermore, they were incorporated into the DfAM decision-making algorithm introduced in Sect. 6, enabling the prediction of the buildability of 3DPF.

4.2 Printability evaluation

In the preliminary printing tests, the printing parameter sets that did not achieve stable material extrusion or sufficient

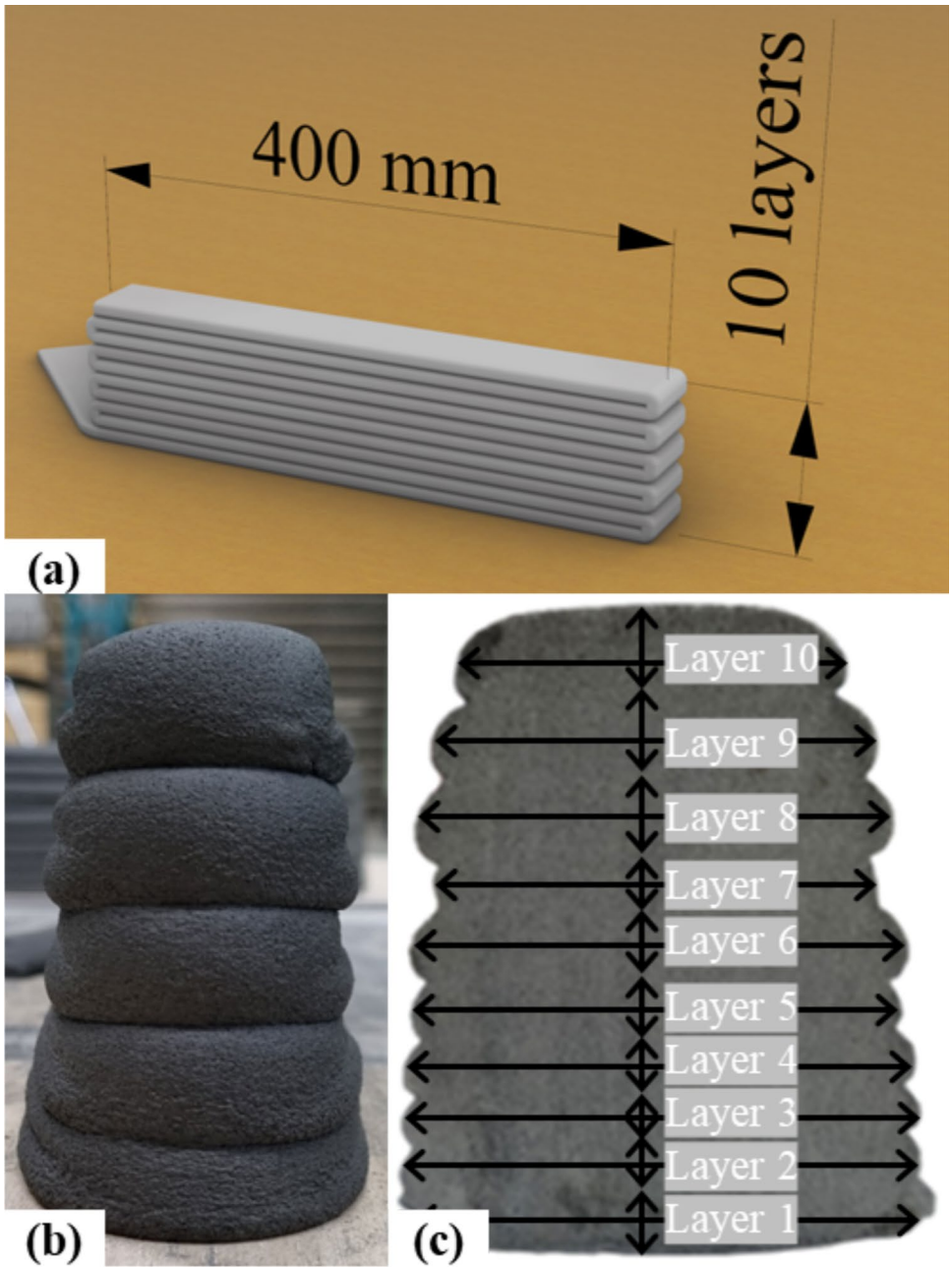


Fig. 10 Layer deformation evaluation: **a** ten-layer single-strip printing model; **b** printed structure; **c** cross-section measurement

layer formation were excluded from the printability evaluation. The printing parameter sets were selected for further testing only when the printed layers exhibited acceptable quality based on direct visual inspection. Specifically, printing parameter sets that resulted in layers deviating from the intended print path, tearing apart, or bursting at the sides owing to excessive extrusion relative to the nozzle diameter were eliminated. The final selection of printing parameters comprised three levels: nozzle speeds of 4000, 4500, and 5000 mm/min; nozzle heights of 8, 10, and 12 mm; and flow rates of 1.8, 2.1, and 2.4 l/min, as summarized in Table 1. A total of 27 printing parameter sets were applied for printability evaluation, based on three variables tested at three levels each.

4.2.1 Layer cross-sectional dimensions

To balance the structural stability and self-weight, the target region was defined as the area where the effective width is relatively large while the cross-sectional area remains small. This region is identified based on the mean values shown in Fig. 12. The mean cross-sectional area was 476.55 mm^2, and the mean effective width was 28.85 mm. As presented in Table 2, the effective width and cross-sectional area

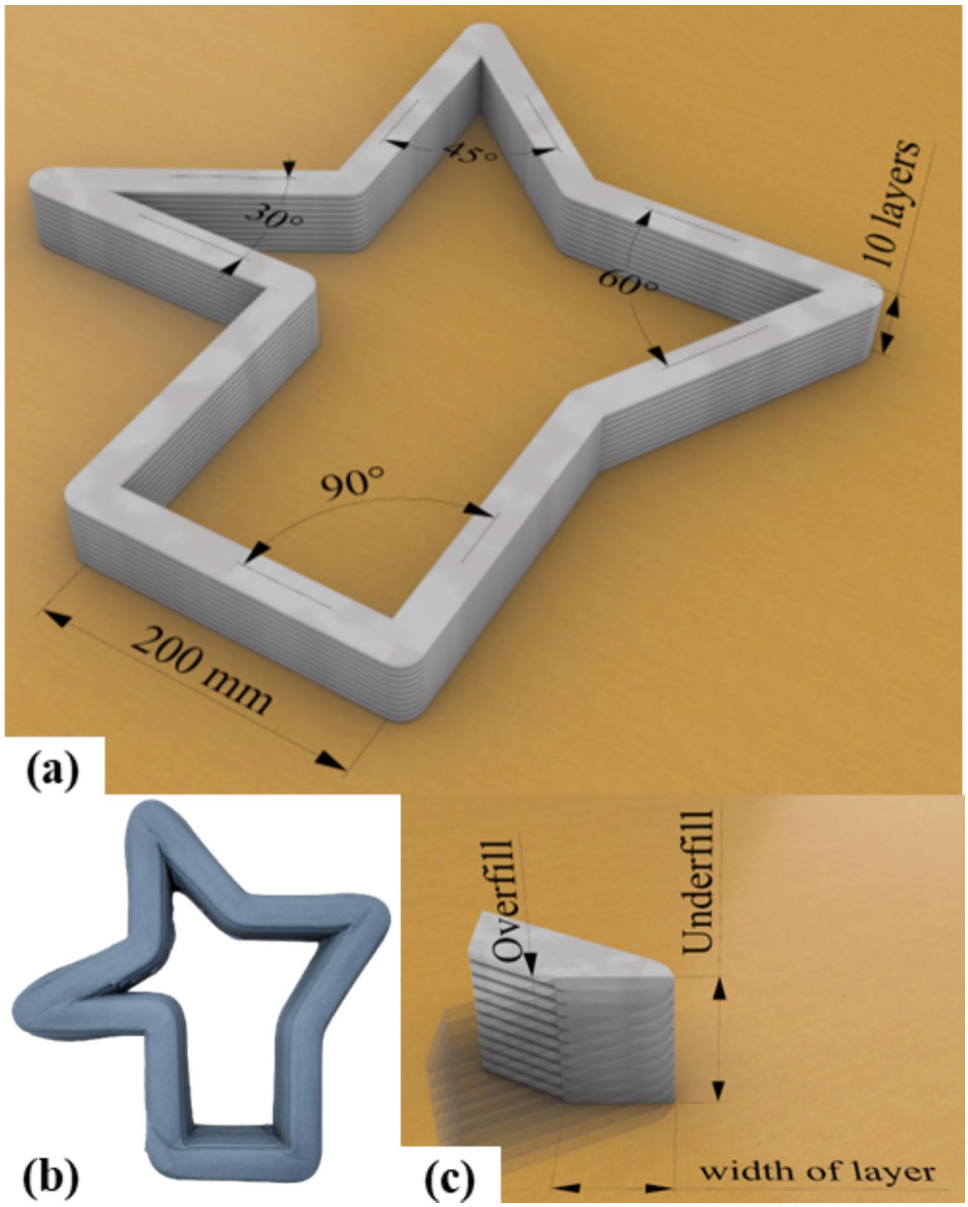


Fig. 11 Evaluation of sharp corners: **a** benchmark structure for evaluating sharp corners; **b** actual printed benchmark structure; **c** measured dimensions

of a single printed layer were measured for each selected set of printing parameters. Four printing parameter sets, 4000/8/1.8, 4500/8/2.4, 5000/8/2.1, and 5000/8/2.4, satisfied the criteria for defining this region and were selected accordingly.

Table 1 Printing parameters identified in preliminary tests for printability evaluation

Level	Nozzle speed (mm/min)	Nozzle height (mm)	Flow rate (l/min)
1	4000	8	1.8
2	4500	10	2.1
3	5000	12	2.4

4.2.2 Buildability

Buildability was evaluated by stacking the maximum number of layers after selecting the printing parameters based on the cross-sectional dimensions of each layer. All printing trials exhibited the same failure mechanism: as the number of layers increased, the yield strength of the material was no longer sufficient to support the self-weight of the stacked layers, causing the structure to gradually lean to one side and eventually collapse because of buckling (Fig. 13). Printing parameter sets 4000/8/1.8 and 4500/8/2.4 achieved a maximum height of 51 layers, while 5000/8/2.0 and 5000/8/2.4 achieved 47 and 46 layers, respectively. Accordingly, the two parameter sets that

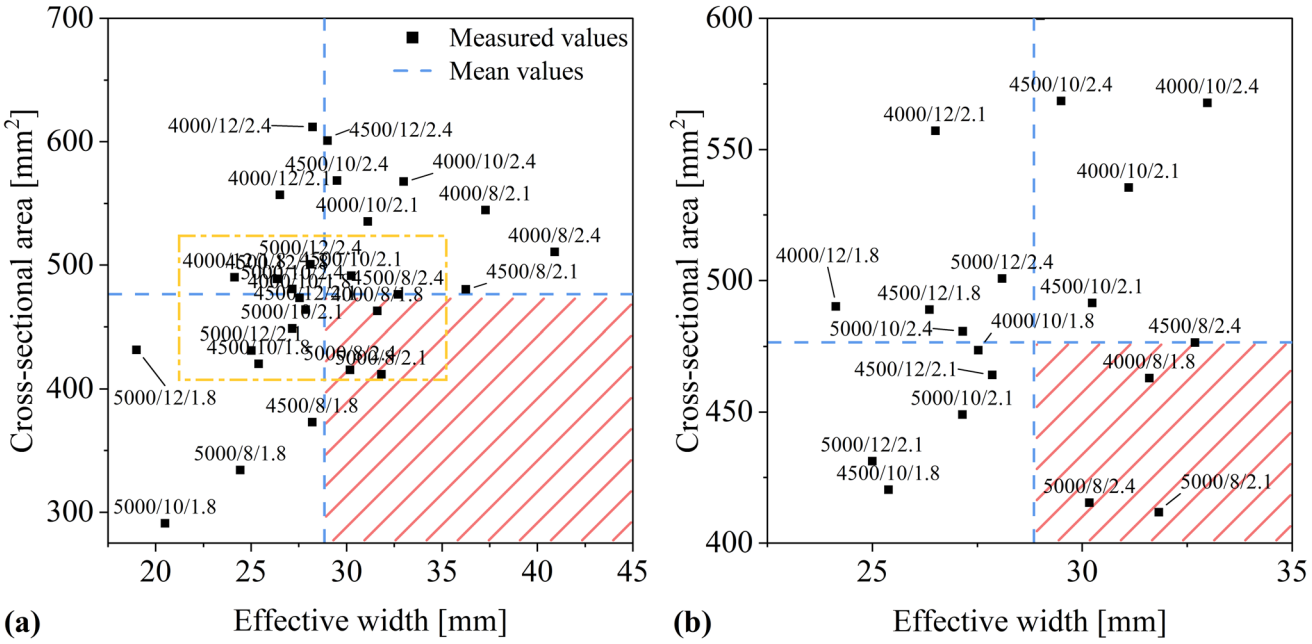


Fig. 12 **a** Distribution of printing parameters based on cross-sectional dimensions of layer; **b** enlarged view of yellow dash-dot rectangular region from original graph

Table 2 Measured layer cross-sectional dimensions of selected printing parameter sets

Printing parameters	Effective width (mm)	Cross-sectional area (mm^2)
4000/8/1.8	31.59	462.97
4500/8/2.4	32.68	476.53
5000/8/2.1	31.82	411.90
5000/8/2.4	30.17	415.47

achieved the greatest height, 4000/8/1.8 and 4500/8/2.4, were selected for further printability evaluation.

4.2.3 Comparison of compressive and flexural strengths of cast and printed specimens

The results of the compressive and flexural strength evaluations for the cast and printed specimens categorized by layer orientation are presented in Fig. 14. Rather than focusing on how the printing parameters affect material strength, this study focused on the practical application of strength data in quality control practice. For compressive strength, all printed specimens exhibited higher values compared with the cast specimens. The lowest compressive strength among the printed specimens was observed in the Z-direction specimen with a 4000/8/1.8 parameter set and was recorded as 30.28 MPa, which is approximately 10% higher than that of



Fig. 13 Buckling failure pattern observed in single-strip printing during buildability evaluation

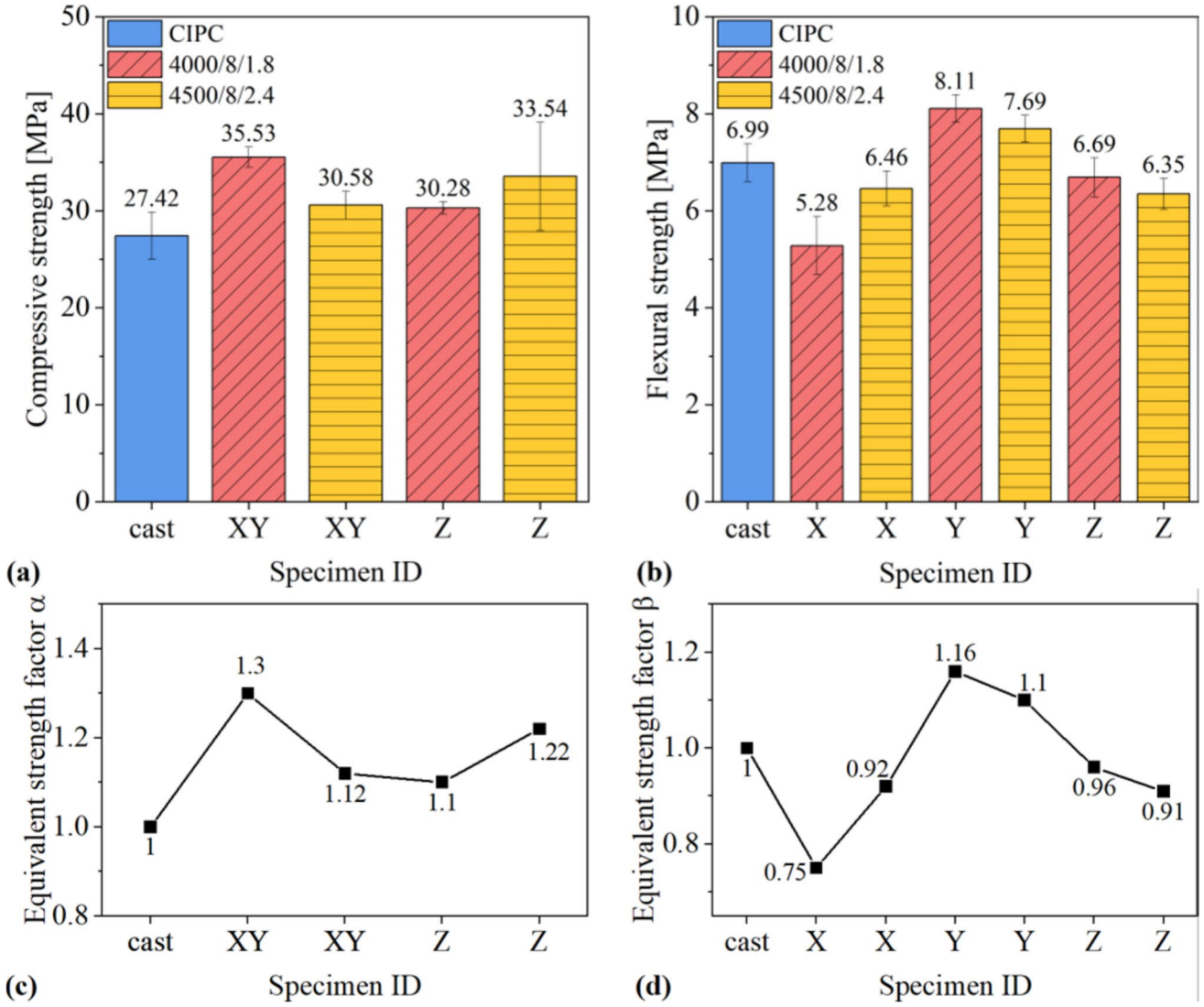


Fig. 14 Comparison of compressive and flexural strength of CIP and printed materials: **a** compressive strength comparison; **b** flexural strength comparison; **c** equivalent strength factor of compressive strength; **d** equivalent strength factor of flexural strength

the cast specimen. For flexural strength, the weakest printed specimen was the X-direction specimen with the 4000/8/1.8 parameter set, exhibiting strength of 5.28 MPa, which is approximately 75% of that of the cast specimen. This indicates that when using this parameter set to manufacture permanent formwork, a conservative design value reduced by 25% is required to achieve structural performance comparable to that of cast components. In contrast, when using the 4500/8/2.4 parameter set, only an 8% reduction in the design strength is necessary. Therefore, 4500/8/2.4 was selected as the printing parameter set in this study. Furthermore, the strength data for all orientations under this parameter set, along with the equivalent strength factor, were used to inform the structural design of the 3DPF and guide periodic quality control based on cast specimen benchmarks.

4.3 Experimental evaluations of geometrical features

To define the geometric constraints associated with the printing parameters selected from the printability evaluation, namely a nozzle speed of 4500 mm/min, a nozzle height of 8 mm, and a flow rate of 2.4 l/min, experimental methods were employed to assess the layer deformation and sharp corners.

4.3.1 Layer deformation

Figure 15 summarizes the evaluation results of layer deformation using the selected printing parameters. Although the seventh layer deviates slightly from the overall trend owing

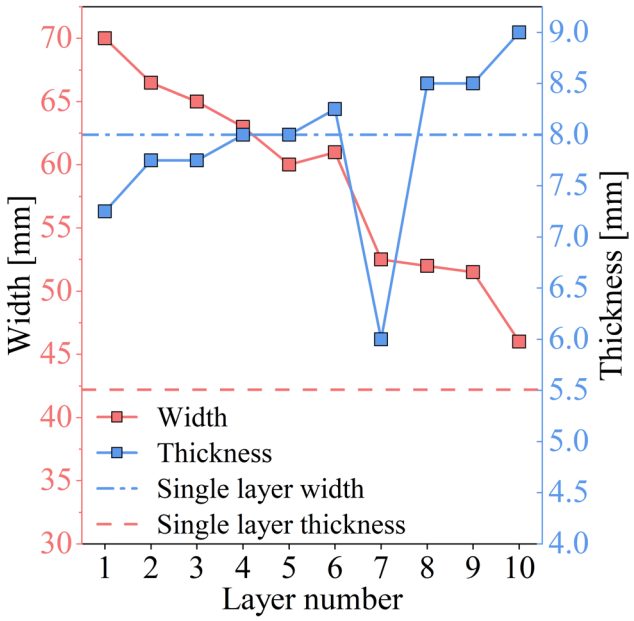


Fig. 15 Measured width and thickness of each printed layer from layer deformation evaluation

to inconsistent material extrusion, a general pattern is evident: as the build progressed, the layer width decreased, and the thickness increased. Compared with the single-layer print, the thicknesses of the fourth, fifth, and sixth layers, located near the middle of the layers, exhibited very similar values.

However, in terms of width, these middle layers exhibit values that are greater by 45%–49% compared with those of the single-layer print. This tendency persists even in the topmost layer, where a similar increase in width is observed. This phenomenon is attributed to the difference in the support conditions: while the base of the single-layer print rests on a flat and level surface, the tenth layer is supported only by the effective width of the tenth layer. In other words, as the layers accumulated, the reduced support area of the underlying structure led to additional lateral deformations.

Because of this layer deformation, the final height of the printed specimen did not reach the target height of 80 mm specified in the design model, but instead measured 79 mm. Therefore, considering the milling joint surface and assembly stages of the 3DPF members, at least one additional layer must be added to the design model to ensure dimensional conformity in actual production.

4.3.2 Effect of sharp corners on layer deformations

Figure 16 illustrates the effect of sharp corners on the printed benchmark structure. In the outer regions of the specimens with corners of 45° and 30°, excessive material extrusion caused the outer edges of the layers to rupture, resulting in visible defects (Fig. 16a).

The total height at the corners tended to increase as the angle decreased because of material over extrusion (Fig. 16b). A noticeable increase in height compared with linear printing began at 60°, while the height variations caused by overfill and underfill remained within 1–2 mm, and did not exhibit obvious dependence on the angle. At 90°, the height reduction caused by the underfill was 77 mm, which was compensated for by adding an additional layer in accordance with the results of the layer deformation evaluation to satisfy the joint surface milling requirements of the permanent formwork.

The width of the first layer also increased as the angle decreased (Fig. 16c). For all corner angles, the measured width was greater than that obtained by linear printing. Regression analysis revealed that exponential regression provided the best fit, and the fitted curve expressed by Eq. (4) is strongly correlated with the experimental data ($R^2 = 0.998$).

$$y = 69.4635 + 270.7784exp(-0.0335x) \tag{4}$$

where y is the width of the first layer, and x is the corner angle. This regression model allows estimating the layer width resulting from material over extrusion at various angles, thereby reducing the need for extensive physical testing.

5 Defined data categories and experimentally collected data for 3DPF manufacturing system

This section introduces an approach for quantitatively managing the quality of a 3DPF manufacturing system based on experimentally collected data and integration between the design and production stages. Table 3 defines the key data categories that must be managed throughout the design and manufacturing processes and organizes the experimental data collected in this study. The table consists of four components (category, unit, data, and type) and highlights the importance of managing these data elements within an integrated framework that reflects their interdependencies, rather than treating them in isolation.

Although the experimental results presented in this study are based on specific materials and conditions, the data categories defined in Table 3 are generalized to ensure applicability across a wide range of environments. Based on these data categories, the proposed framework can be structured to systematically assess and reflect quality throughout the 3DPF design-to-manufacturing process.

The properties of fresh materials can be used throughout the design, manufacturing planning, and quality control

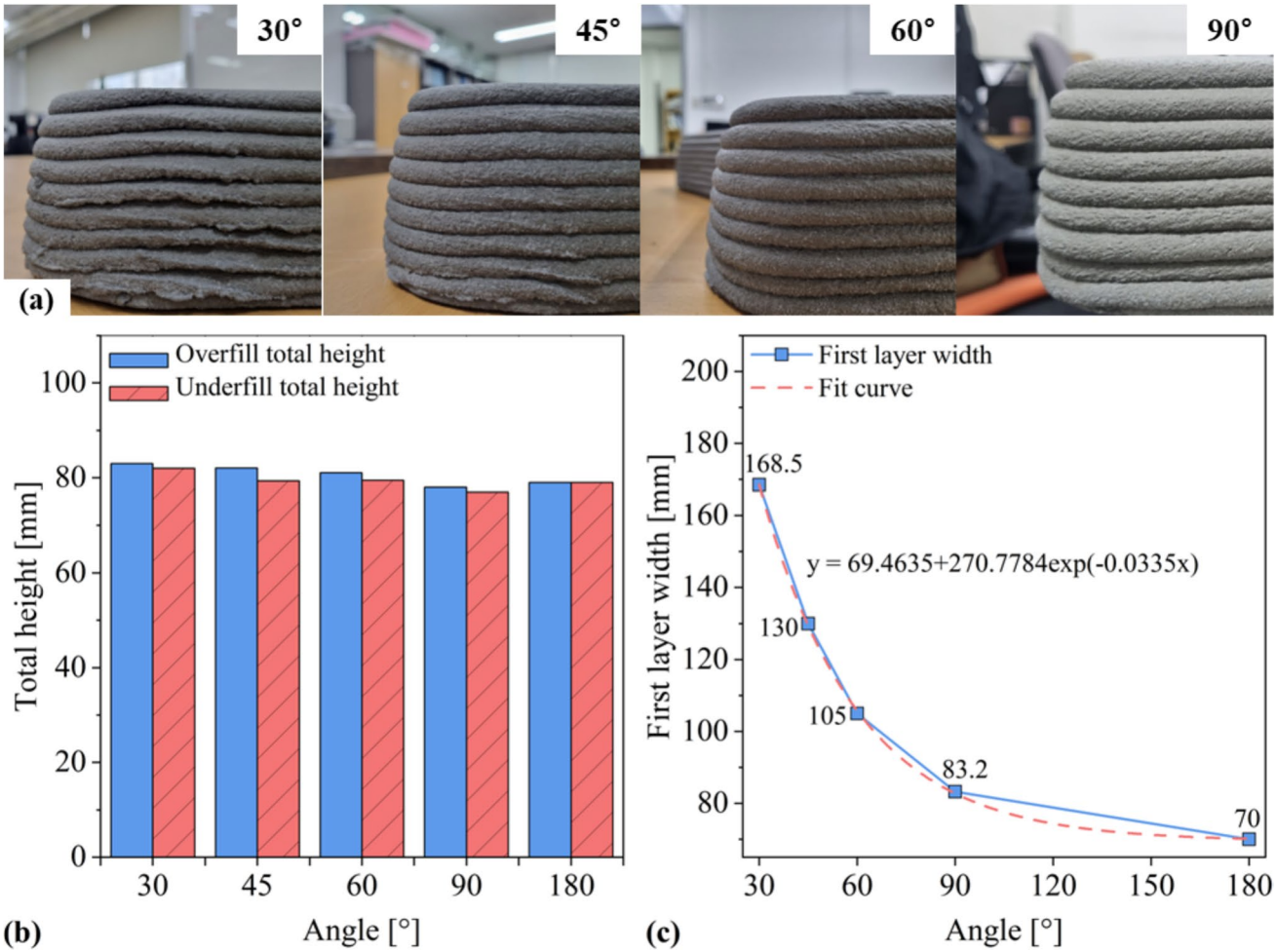


Fig. 16 Effect of sharp angles on layer geometry in 3D concrete printing: **a** printed specimen containing multiple sharp angles; **b** total height variation with overfill and underfill distribution; **c** variation of first layer width with sharp angles

stages. The key indicators used to evaluate buildability include material density and rheological properties, such as the initial dynamic yield shear stress, re-flocculation rate (R_{thix}), initial static yield shear stress, and structuration rate (A_{thix}), as noted by Kruger et al. [12]. These properties are discussed in detail in Sect. 6. This dataset serves as a reference for verifying whether the target fresh material properties were achieved immediately after mixing and directly influences the selection of printing parameters, application of geometrical constraints, and prediction of hardened material strength.

Printing parameters must be explicitly incorporated into both the design and manufacturing planning stages and serve as key indicators for evaluating buildability, particularly in conjunction with fresh material properties [50]. These parameters are influenced not only by material characteristics but also by environmental conditions and ultimately affect the equivalent strength factor and geometrical constraints [43, 45, 51]. By considering both the fresh material properties and printing parameters, the maximum printable height for a given geometry can be estimated in advance [12, 13]. This information should be systematically linked to a design model for effective integration and control.

The hardened material strength was used during both the design and quality control stages in the manufacturing process. The strength of the printed material serves as the basis for designing the structural cross-section of the permanent formwork [42], and the anisotropy caused by the layer-by-layer deposition process can be corrected using the equivalent strength factor. For in-process quality control, it is effective to periodically evaluate the strength using cast specimens rather than printed specimens and compare the results with the reference values listed in Table 3. This category is influenced by the fresh material properties, environmental conditions, and printing parameters [45].

Geometrical constraints are applied during the design and manufacturing planning stages to assess whether a given geometry is printable and evaluate the need for

Table 3 Data categories and corresponding collected data for quality control in 3DPF manufacturing system

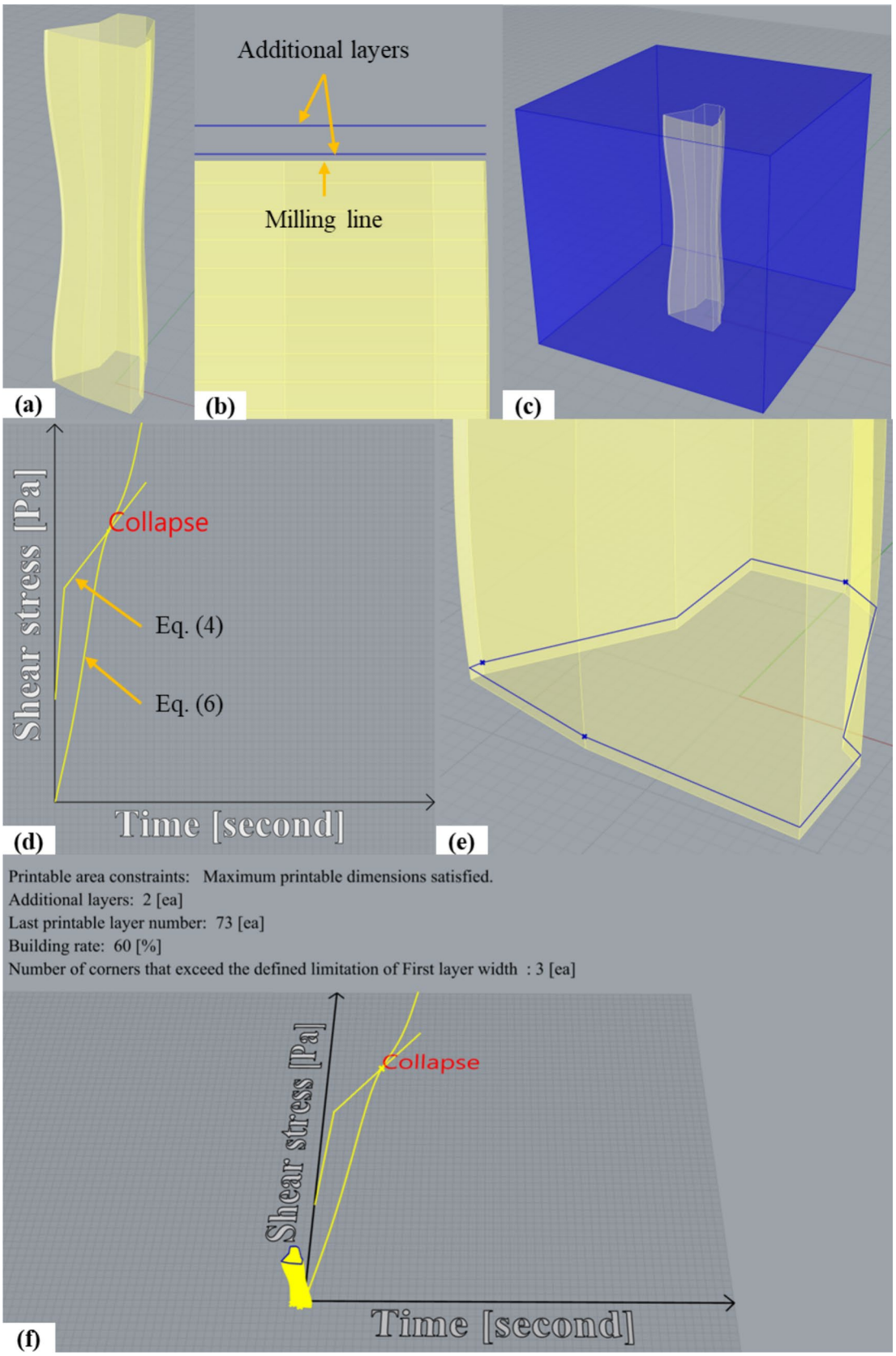
Category	Unit	Data	Type
A. Fresh material properties			
$\tau_{D,i}$	Pa	1356.1	Numeric
R_{thix}	Pa/s	12.3	Numeric
$\tau_{S,i}$	Pa	2832.1	
A_{thix}	Pa/s	1.3	Numeric
Material density	Kg/m^3	2219.7	Numeric
B. Printing parameters			
Nozzle shape	-	Circle	Text
Nozzle diameter	mm	22	Numeric
Nozzle speed	mm/min	4500	Numeric
Nozzle height	mm	8	Numeric
Flow rate	l/mm	2.4	Numeric
C. Hardened material strengths			
$f_{cm,cast}$	MPa	27.42	Numeric
XY-direction equivalent strength factor	-	1.12	Numeric
Z-direction equivalent strength factor	-	1.22	Numeric
$f_{rm,cast}$	MPa	6.99	Numeric
X-direction equivalent strength factor	-	0.92	Numeric
Y-direction equivalent strength factor	-	1.10	Numeric
Z-direction equivalent strength factor	-	0.91	Numeric
D. Geometrical constraints			
Additional layers for milling	ea	2	Numeric
First layer width from sharp angles	mm	$69.4635+270.7784exp(-0.0335x)$	Equation
Maximum printable dimension (X)	mm	1000	Numeric
Maximum printable dimension (Y)	mm	1000	Numeric
Maximum printable dimension (Z)	mm	1000	Numeric
E. Environmental conditions			
Temperature	°C	15.2 ± 1	Numeric
Humidity	%	61 ± 1	Numeric

postprocessing or design modification. In this study, the number of additional milling layers was set to two. This includes the following: (1) one layer to compensate for the height reduction caused by layer deformation, (2) one layer to correct for residual height discrepancies when the total height of the printing model is not an exact multiple of the nozzle height during slicing.

First-layer deformation near sharp corners can interfere with internal reinforcement or external structural elements. Accordingly, Sect. 6 discusses three possible strategies for using sharp-angle data in design and production planning: (1) applying only corner angles that do not interfere with reinforcement details and fall within acceptable assembly tolerances, (2) enabling subtractive fabrication of both the inner and outer surfaces to eliminate interference with embedded components, (3) modifying the printing model using methods such as corner rounding [52] or adjusting the nozzle speed [53].

Additionally, the maximum XYZ dimensions serve as a constraint for the printable dimensions of the 3DPF and must be considered when planning segmentation and assembly. Among all data categories, the geometrical constraints are influenced by all other categories, but do not exert influence in return, making them the final category to be defined. Rather than being managed as isolated numerical values, the geometric constraint categories should be handled using a DfAM approach that is closely integrated with the design model.

Environmental conditions play a critical role in the quality control phases of manufacturing. Temperature and humidity significantly affect the overall quality by influencing the material extrusion, layer deposition, and interlayer bonding strength; therefore, they must be continuously monitored throughout the printing process [54]. Because environmental conditions directly affect the


Additional layers
Milling line
(a)
(b)
(c)
Shear stress [Pa]
Collapse
Eq. (4)
Eq. (6)
Time [second]
(d)
(e)
Printable area constraints: Maximum printable dimensions satisfied.
Additional layers: 2 [ea]
Last printable layer number: 73 [ea]
Building rate: 60 [%]
Number of corners that exceed the defined limitation of First layer width : 3 [ea]
Shear stress [Pa]
Collapse
Time [second]
(f)

◂**Fig. 17** Examples of results obtained by DfAM decision-making algorithm: **a** example 3DPF design model; **b** additional print paths generated for milling process; **c** plastic collapse prediction; **d** verification of printable dimensions; **e** prediction of first layer width at sharp corners; **f** summary report for manufacturability evaluations

material properties, they function as governing variables that influence all other data categories.

6 Utilization of the experimental data in DfAM decision-making algorithm

If the collected data presented in Table 3 are linked to the design model, it is possible to enhance the quality of the 3DPF before the manufacturing stage. This chapter proposes a DfAM decision-making algorithm to convert the design model into a printing model based on the data collected and analyzed in the preceding experiments. A design algorithm was developed using Grasshopper, which is a parametric design tool in Rhinoceros 3D (Robert McNeel & Associates, USA), to evaluate the manufacturability of a specific 3DPF design model based on the experimental data.

When a design model is input into the algorithm, it is converted into contours for the printing path. Based on the collected data, the algorithm sequentially generates additional layers for top surface milling and evaluates the maximum printable dimensions, plastic collapse height prediction, and first-layer width variation caused by sharp corners. The evaluation results can serve as a quantitative reference for pre-manufacturing evaluations, enabling practitioners to establish more reliable production plans for high-quality 3DPF fabrication.

Figure 17 shows the evaluation results for a 3DPF design example using the parametric algorithm developed in this study. First, the final contour extracted from the design model is vertically offset by the nozzle height and duplicated according to the number of additional layers for milling defined in Table 3 (Fig. 17b). These layers, which enable surface milling to improve the quality of the joint interfaces and correct height discrepancies, were subsequently incorporated into the model. Then, the algorithm evaluated the maximum printable dimensions, plastic collapse, and sharp corners.

Next, this study evaluated whether the converted design model intersected the printable region defined by the maximum printable dimensions (X, Y, Z) listed in Table 3 (Fig. 17c). In the design example, the original model height was 950 mm. With the addition of two layers for top-surface milling, the total height increased to 966 mm. In Fig. 17c, the blue bounding box represents the printable region defined by the maximum printable dimensions of 1000 mm × 1000 mm × 1000 mm. Because the modified design model did not exceed these limits, the evaluation proceeded to the next step. However, if any part of the model exceeds this region, the segmentation of the 3DPF must be reconsidered based on the structural behavior of the member before proceeding to the subsequent evaluation.

If the converted design model satisfies the maximum printable dimensions, the next step is to assess buildability. Kruger et al. [12] predicted the plastic collapse in a cylindrical printing model by identifying the point at which the increasing self-weight of the printed layers exceeded the time-dependent evolution of yield stress. Their mathematical model was implemented in the parametric modeling tool developed in this study. Although buildability was evaluated using cylindrical printing models with uniform print path lengths in the previous study, the proposed DfAM decision-making algorithm enabled the prediction of the lower boundary for plastic collapse in freeform 3DPF geometries by calculating the length and printing speed of each individual layer. By linking the design data with the manufacturing system, this approach allowed for the computation of layer-specific self-weight accumulation and yield stress development, thereby extending the previous methodology to nonuniform geometries.

To predict the plastic collapse in free-form 3DPF design models, Eqs. (5)–(7) were implemented in the algorithm. Equation (5) defines the static yield shear stress of the material as a function of time after extrusion and cessation of agitation. Initially, the yield shear stress increased from the dynamic yield shear stress, exhibiting a short-term increase governed by the re-flocculation rate. After the re-flocculation time t_{rf} (Eq. (6)), the stress continued to increase from the static yield shear stress, with time-dependent growth governed by the structuration rate. Although Kruger et al. [12] used a constant printing path length for each layer in their cylindrical model, this study modified the model to accommodate the printing path length of the kth layer and redefined the deposition time interval as the period between the completion of the $(k-1)$th and kth layers. This adaptation enabled the application of the equations to geometries with nonuniform layer paths Eq. (7).

$$\tau_S(t) = \begin{cases} \tau_{D,i} + R_{thix} \cdot t, \left(t \le t_{rf}\right) \\ \tau_{S,i} + A_{thix} \cdot \left(t - t_{rf}\right), \left(t_{rf} < t\right) \end{cases} \tag{5}$$

$$t_{\mathrm{rf}} = \frac{\tau_{\mathrm{S,i}} - \tau_{\mathrm{D,i}}}{R_{\mathrm{thix}}} \tag{6}$$

$$\tau_B(t) = \frac{h_l \cdot \rho \cdot g \cdot 10^{-3} \cdot v}{2 \cdot F_{AR} \cdot l_k} \cdot t\left(\sum_{x=1}^{k-1} \frac{l_x}{v} \le t < \sum_{x=1}^{k} \frac{l_x}{v}\right) \tag{7}$$

The parameters are defined as follows:

$\tau_S(t)$ Static yield shear stress of material at time t after agitation (Pa)

$\tau_{D,i}$ Initial dynamic yield shear stress of printing material (Pa)

R_{thix} Re-flocculation rate (Pa/s)

t Time since cessation of agitation (s)

t_{rf} Time period during which re-flocculation occurs and dominant shear stress increases (s)

$\tau_{S,i}$ Initial static yield shear stress of printing material (Pa)

A_{thix} Structuration rate (Pa/s)

$\tau_B(t)$ Building rate (Pa)

h_l Layer height (mm)

ρ Material density (kg/m^3)

g Gravitational constant equal to 9.81 (m/s^2)

v Nozzle speed (mm/s)

F_{AR} Strength correction factor that accounts for confinement resulting from smaller aspect ratios (aspect ratio is h_l/w_l)

w_l Effective layer width (mm)

l_k Printing path length of kth layer

The parameters used in Eqs. (5)–(7) were assigned based on the structured data categories defined in this study. Material-related parameters, such as the initial dynamic and static yield shear stresses, re-flocculation rate, and structuration rate, were sourced from the *Fresh material properties* category. The parameters used to compute the building rate, including the layer height, nozzle speed, and strength correction factor, were derived from the *Printing parameters* category. The effective layer width was determined based on the selected printing parameters, and the printing path length for each layer was extracted from the contours of the validated design model. Figure 17d presents a comparison between the time-dependent development of the static yield shear stress and the accumulated self-weight of each layer calculated according to the input design model. The results indicate that plastic collapse is expected before the target height is reached. This outcome was confirmed in the final reporting stage of the algorithm.

Figure 17e shows the predicted first-layer width at the sharp corners of the 3DPF model. This algorithm applies a regression equation derived from earlier sharp-corner experiments (Eq. (4)) to automatically calculate the angle at each corner of the given design model. These angles were substituted into Eq. (4) to quantitatively estimate the corresponding first-layer width. If the predicted width exceeded a predefined threshold in terms of the first layer width, the corresponding corner was flagged as a critical point. In the example model, the threshold was evaluated by specifying the width of x mm as a constraint criterion. This approach allows for the early detection and resolution of potential geometrical issues caused by sharp corners during the design stage.

Finally, Fig. 17f presents a summary report of the evaluation results, for the example 3DPF model. This report consolidates the results of the proposed algorithm to support DfAM practitioners in making informed decisions. Based on the results, although the design model fits within the defined printable dimensions, it is expected that it will undergo plastic collapse in the 73rd layer, corresponding to a buildability ratio of 60%. In such cases, it is recommended to divide the model into predicted failure layers and adopt a segmented assembly approach using two joined segments. Additionally, the algorithm identified three sharp corners where the predicted width for the first layer width exceeded the assumed sharp corner constraint threshold. For these critical points, appropriate mitigation strategies such as those proposed in Sect. 6 for sharp corner compensation should be considered during design refinement.

The proposed DfAM decision-making algorithm integrates experimentally collected data with a design model to evaluate the manufacturability of 3DPF before printing. By automating the assessment of additional layers, maximum printable dimensions, plastic collapse, and sharp corners, the algorithm provides a consistent basis for adjusting the printing model, thereby supporting improved quality control in the 3DPF manufacturing process. This algorithm is available at https://github.com/rlaxo1022/DfM-method-for-3DCP.

7 Conclusions

This study developed an experimental data–driven framework to ensure the quality of 3DPF. The main contribution of this study is the incorporation of experimental data into the DfAM-based design and manufacturing processes, enabling systematic quality control and a stable manufacturing system for 3DPF. The proposed framework integrates

systematic experimental evaluations of the manufacturing process, structured data collection, and a DfAM decision-making algorithm, offering a unified approach for managing material properties, printing parameters, and design constraints. The main conclusions drawn from this study are as follows:

1. A systematic experimental methodology was developed and implemented to collect essential data for 3DPF quality control. This methodology includes the evaluation of rheological properties, selection of appropriate printing parameters, and assessment of geometrical constraints. Specifically, to address the anisotropic strength of the printed material effectively, an equivalent strength factor is proposed based on comparisons with cast specimens. Furthermore, the increase in the first-layer width at sharp corners exhibited an exponential relationship with the decreasing corner angles.
2. The quantitative quality control of the 3DPF manufacturing system was achieved through a systematic collection of experimental data corresponding to five essential data categories: fresh material properties, printing parameters, hardened material strength, geometrical constraints, and environmental conditions. This data was not managed independently but were instead coordinated in an integrated manner accounting for their interdependence. By linking these data categories to the design model, the proposed framework enables the prediction and incorporation of manufacturability and quality at the early design stage. Although the dataset was derived under specific experimental conditions, the proposed framework can be extended to a general quality management system applicable to various environments. Furthermore, the framework was integrated with the DfAM decision-making algorithm, expanding its role in the design phase of digital fabrication workflows.
3. A DfAM decision-making algorithm is proposed to use the data collected during the design stage. This algorithm facilitates the transformation of a design model into a printable manufacturing model through functions such as generating additional layers for milling, predicting buildability, evaluating the maximum printable dimensions, and estimating the width of the first layer at sharp corners. This approach facilitates the proactive identification and mitigation of potential manufacturing failures and quality deficiencies, thereby contributing to the establishment of a DfAM process that enables experimental data–driven decision making in early design stages.

Although the experimental results were derived from a specific combination of materials and equipment, the defined data categories and proposed DfAM decision-making algorithm are not limited to these conditions. The proposed framework can be expanded to new materials, different printing setups, and applications beyond 3DPF, such as construction strategies that employ infill structures instead of perimeter-type geometries. Defining the minimum quality criteria for each data category or establishing valid parameter ranges based on their interrelationships will further support the implementation of more robust and constrained manufacturing systems. Nevertheless, its capacity to predict global deformation or strength remains limited, since the framework was validated using small-scale benchmark structures.

Continued data accumulation and the integration of AI-based methods into parametric algorithms can enhance the reliability of manufacturability assessments across various design and material contexts. Furthermore, because this study aimed to establish a digital fabrication workflow that integrates 3D concrete printing and robotic milling, follow-up studies on equipment development and surface finishing methodologies are crucial for realizing high precision 3DPF manufacturing.

Author contribution Tae-Kyung Kim: conceptualization, data collection, formal analysis, writing—original draft, writing—review and editing, and funding acquisition. Sangwoo Oh: original draft, data collection, formal analysis. Jinsuk Lee: data collection, formal analysis. Seongcheol Choi: supervision. Chang-Su Shim: funding acquisition, supervision.

Funding Open Access funding enabled and organized by Chung-Ang University. This study was supported by the National R&D Project for Smart Construction Technology (RS-2020-KA156007) funded by the Korea Agency for Infrastructure Technology Advancement under the Ministry of Land, Infrastructure and Transport, and managed by the Korea Expressway Corporation. Additionally, this study was supported by the Basic Science Research Program through the National Research Foundation of Korea (NRF), funded by the Ministry of Education (RS-2024-00407741).

Data availability The data that support the findings of this study are available from the corresponding author, Chang-Su Shim, upon reasonable request.

Declarations

Conflict of interest The authors declare no competing interests.

Open Access This article is licensed under a Creative Commons Attribution-NonCommercial-NoDerivatives 4.0 International License, which permits any non-commercial use, sharing, distribution and reproduction in any medium or format, as long as you give appropriate credit to the original author(s) and the source, provide a link to the Creative Commons licence, and indicate if you modified the licensed material. You do not have permission under this licence to share adapted material derived from this article or parts of it. The images or other third party material in this article are included in the article's Creative Commons licence, unless indicated otherwise in a credit line to the material. If material is not included in the article's Creative Commons licence and

your intended use is not permitted by statutory regulation or exceeds the permitted use, you will need to obtain permission directly from the copyright holder. To view a copy of this licence, visit http://creativecommons.org/licenses/by-nc-nd/4.0/.

References

1. Ahmed Z, Wolfs R, Bos F, Salet T (2022) A framework for large-scale structural applications of 3D printed concrete: the case of a 29 m bridge in the Netherlands. Open Conference Proceedings 1:5–19
2. Salet T, Ahmed Z, Bos F, Laagland HLM (2018) Design of a 3d printed concrete bridge by testing. Virtual Phys Prototyp 13(3):222–236. https://doi.org/10.1080/17452759.2018.1476064
3. Breseghello L, Naboni R (2022) Toolpath-based design for 3D concrete printing of carbon-efficient architectural structures. Addit Manuf 56:102872. https://doi.org/10.1016/j.addma.2022.102872
4. Saqib A, Dieg A, Max W, Giovanni B, Christoph G (2021) Towards a multifunctional 3DCP slab system. Int Conf Spat Struct 2020(21):2021
5. Jipa A, Dillenburger B (2022) 3D printed formwork for concrete: state-of-the-art, opportunities, challenges, and applications. 3D Print Addit Manuf 9(2):84–107. https://doi.org/10.1089/3dp.2021.0024
6. Qiu M, Qian Y, Dai JG (2024) Enhancing the flexural performance of concrete beams with 3D-printed UHP-SHCC permanent formwork via graded fiber volume fraction. Compos Struct. https://doi.org/10.1016/j.compstruct.2024.118211
7. Farahbakhsh M, Rybkowski ZK, Zakira U, Kalantar N, Onifade I (2022) Impact of robotic 3D printing process parameters on interlayer bond strength. Autom Constr 142:104478. https://doi.org/10.1016/j.autcon.2022.104478
8. Wolfs R (2019) Interlayer adhesion and strength of modelling of 3D printed concrete: controlling structural behaviour in the fresh and hardened state. Dissertation, Technische Universiteit Eindhoven
9. Zareiyan B, Khoshnevis B (2017) Interlayer adhesion and strength of structures in Contour Crafting: effects of aggregate size, extrusion rate, and layer thickness. Autom Constr 81:112–121. https://doi.org/10.1016/j.autcon.2017.06.013
10. Nerella VN, Näther M, Iqbal A, Butler M, Mechtcherine V (2019) Inline quantification of extrudability of cementitious materials for digital construction. Cem Concr Compos 95:260–270. https://doi.org/10.1016/j.cemconcomp.2018.09.015
11. Jhun J, Lee DH, Rehman AU, Kang S, Kim JH (2024) Development of a real-time geometric quality monitoring system for extruded filaments of 3D concrete printing construction. IEEE Access 23:69981–69999. https://doi.org/10.1109/ACCESS.2024.3401472
12. Kruger J, Zeranka S, van Zijl G (2019) 3D concrete printing: a lower bound analytical model for buildability performance quantification. Autom Constr 106:102904. https://doi.org/10.1016/j.autcon.2019.102904
13. Kruger J, Cho S, Zeranka S, Viljoen C, van Zijl G (2020) 3D concrete printer parameter optimisation for high rate digital construction avoiding plastic collapse. Compos Part B Eng 183:107660. https://doi.org/10.1016/j.compositesb.2019.107660
14. Xiao J, Bai M, Wu Y, Duan Z, Qin J (2024) Interlayer bonding strength and pore characteristics of 3D printed engineered cementitious composites (ECC). J Build Eng 84:108559. https://doi.org/10.1016/j.jobe.2024.108559
15. Mostert JP, Kruger J (2025) Reducing anisotropic behaviour of 3D printed concrete through interlocked filaments. Mater Struct 58:192. https://doi.org/10.1617/s11527-025-02723-9
16. Cui W, Sun H, Zhou J (2024) Geometric quality evaluation of three-dimensional printable concrete using computational fluid dynamics. Front Struct Civ Eng 18:963–976. https://doi.org/10.1007/s11709-024-1080-4
17. Dobrzanski J, Xu J, Bartek R, De Becker D, Kinnell P, Kolawole J, Konstantatou M, Maddock R, Isa MN, Sehlstedt V, Buswell R (2025) From digital crafting to digital manufacturing: automated production using hybrid 3D concrete printing. J Build Eng 108:112640. https://doi.org/10.1016/j.jobe.2025.112640
18. Thompson MK, Moroni G, Vaneker T, Fadel G, Campbell RI, Gibson I et al (2016) Design for additive manufacturing: trends, opportunities, considerations, and constraints. CIRP Ann 65(2):737–760. https://doi.org/10.1016/j.cirp.2016.05.004
19. Yang W, Wang L, Ma G, Feng P (2023) An integrated method of topological optimization and path design for 3D concrete printing. Eng Struct 291:116435. https://doi.org/10.1016/j.engstruct.2023.116435
20. Dell'Endice A, Bouten S, Van Mele T, Block P (2023) Structural design and engineering of Striatus, an unreinforced 3D-concrete-printed masonry arch bridge. Eng Struct 292:116534. https://doi.org/10.1016/j.engstruct.2023.116435
21. Weng Y, Mohamed NAN, Lee BJS, Gan NJH, Li M, Tan MJ et al (2021) Extracting BIM information for lattice toolpath planning in digital concrete printing with developed dynamo script: a case study. J Comput Civ Eng 35(3):05021001. https://doi.org/10.1061/(ASCE)CP.1943-5487.0000964
22. Davtalab O, Kazemian A, Khoshnevis B (2018) Perspectives on a BIM-integrated software platform for robotic construction through Contour Crafting. Autom Constr 89:13–23. https://doi.org/10.1016/j.autcon.2018.01.006
23. Ding L, Wei R, Che H (2014) Development of a BIM-based automated construction system. Procedia Eng 85:123–131. https://doi.org/10.1016/j.proeng.2014.10.536
24. Kim TK, Nguyen DC, Shim CS (2022) Digital fabrication for DfMA of a prefabricated bridge pier. In: Proceedings of the 17th East Asian-Pacific Conference on Structural Engineering and Construction (EASEC-17), Singapore. Springer Nature Singapore, pp 305–310. https://doi.org/10.1007/978-981-19-7331-4_24
25. Chen Q, Gao Y, Ding L, Zhou C, Han W, Zhou Y, Shi Y (2023) Genetic algorithm–based multiobjective optimization for 3D printable design of a double-shell lunar habitat structure. J Aerosp Eng 36(6):04023069. https://doi.org/10.1061/JAEEEZ.ASENG-47
26. Bi M, Tran P, Xia L, Ma G, Xie YM (2022) Topology optimization for 3D concrete printing with various manufacturing constraints. Addit Manuf 57:102982. https://doi.org/10.1016/j.addma.2022.102982
27. Giridhar G, Prem PR, Kumar S (2023) Development of concrete mixes for 3D printing using simple tools and techniques. Sādhanā 48(1):16. https://doi.org/10.1007/s12046-022-02069-w
28. Oh S, Hong G, Choi S (2021) Literature review on rheological properties and required performances of 3D printable cementitious materials. J Korean Recycl Constr Resour Inst 9(1):41–49. https://doi.org/10.14190/JRCR.2021.9.1.41
29. Zhang C, Nerella VN, Krishna A, Wang S, Zhang Y, Mechtcherine V, Banthia N (2021) Mix design concepts for 3D printable concrete: a review. Cem Concr Compos 122:104155. https://doi.org/10.1016/j.cemconcomp.2021.104155
30. Le TT, Austin SA, Lim S, Buswell RA, Gibb AGF, Thorpe T (2012) Mix design and fresh properties for high-performance printing concrete. Mater Struct 45:1221–1232. https://doi.org/10.1617/s11527-012-9828-z
31. Ma G, Li Z, Wang L (2018) Printable properties of cementitious material containing copper tailings for extrusion based 3D printing. Constr Build Mater 162:613–627. https://doi.org/10.1016/j.conbuildmat.2017.12.051

32. Zhang Y, Zhang Y, She W, Yang L, Liu G, Yang Y (2019) Rheological and hardened properties of the high-thixotropy 3D printing concrete. Constr Build Mater 201:278–285. https://doi.org/10.1016/j.conbuildmat.2018.12.061
33. Marchon D, Kawashima S, Bessaies-Bey H, Mantellato S, Ng S (2018) Hydration and rheology control of concrete for digital fabrication: potential admixtures and cement chemistry. Cem Concr Res 112:96–110. https://doi.org/10.1016/j.cemconres.2018.05.014
34. Korean Standards Association (KSA) (2001) Portland cement, KS L 5201
35. Korean Standards Association (KSA) (2023) Fly ash, KS L 5405
36. ASTM International (2007) ASTM C1437–07: standard test method for flow of hydraulic cement mortar. West Conshohocken, PA
37. ASTM International (2020) ASTM C403/C403M-20: standard test method for time of setting of concrete mixtures by penetration resistance. West Conshohocken, PA, USA
38. Roussel N (ed) (2011) Understanding the rheology of concrete. Elsevier
39. Dzuy NQ, Boger DV (1983) Yield stress measurement for concentrated suspensions. J Rheol 27(4):321–349. https://doi.org/10.1122/1.549709
40. ASTM International (2005) ASTM C109/C109M-05: Standard test method for compressive strength of hydraulic cement mortars (using 2-in. or [50-mm] cube specimens). Annual Book of ASTM Standards, Vol. 04.01. West Conshohocken, PA.
41. ASTM International (2019) ASTM C348–18: Standard test method for flexural strength of hydraulic cement mortars. West Conshohocken, PA, USA
42. Kim TK, Oh S, Lee J, Dong WJ, Bunleang M, Choi S, Shim CS (2025) Effects of 3D-printed concrete permanent formwork on the flexural behavior of reinforced concrete beams: experimental and analytical investigations. Case Stud Constr Mater 22. https://doi.org/10.1016/j.cscm.2025.e04802
43. Chandra PS, Basit MA, Hasan NMS, Dey D, Panda B (2023) 3D printing of geopolymer mortar: overview of the effect of mix design and printing parameters on the strength. Mater Today Proc. https://doi.org/10.1016/j.matpr.2023.04.292
44. Zhang N, Sanjayan J (2023) Extrusion nozzle design and print parameter selections for 3D concrete printing. Cem Concr Compo 137:104939. https://doi.org/10.1016/j.cemconcomp.2023.104939
45. Wolfs RJM, Bos FP, Salet TAM (2019) Hardened properties of 3D printed concrete: the influence of process parameters on interlayer adhesion. Cem Concr Res 119:132–140. https://doi.org/10.1016/j.cemconres.2019.02.017
46. Suiker ASJ (2018) Mechanical performance of wall structures in 3D printing processes: theory, design tools and experiments. Int J Mech Sci 137:145–170. https://doi.org/10.1016/j.ijmecsci.2018.01.010
47. Suiker AS, Wolfs RJ, Lucas SM, Salet TA (2020) Elastic buckling and plastic collapse during 3D concrete printing. Cem Concr Res 135:106016. https://doi.org/10.1016/j.cemconres.2020.106016
48. Schneider CA, Rasband WS, Eliceiri KW (2012) NIH Image to ImageJ: 25 years of image analysis. Nat Methods 9(7):671–675
49. Roussel N (2018) Rheological requirements for printable concretes. Cem Concr Res 112:76–85. https://doi.org/10.1016/j.cemconres.2018.04.005
50. Khan SA, Koç M (2023) Buildability analysis of 3D concrete printing process: a parametric study using design of experiment approach. Processes 11(3):782. https://doi.org/10.3390/pr11030782
51. Zhang N, Sanjayan J (2023) Extrusion nozzle design and print parameter selections for 3D concrete printing. Cem Concr Compos 137:104939. https://doi.org/10.1016/j.cemconcomp.2023.104939
52. Comminal R, Serdeczny MP, Pedersen DB, Spangenberg J (2019) Motion planning and numerical simulation of material deposition at corners in extrusion additive manufacturing. Addit Manuf 29:100805. https://doi.org/10.1016/j.addma.2019.06.005
53. Mohite AA (2021) Speed-based additive manufacturing technique: discovery and exploration of design potential of speed of deposition in additive manufacturing. Dissertation, Aalto University.
54. Shoukry SN, William GW, Downie B, Riad MY (2011) Effect of moisture and temperature on the mechanical properties of concrete. Constr Build Mater 25(2):688–696. https://doi.org/10.1016/j.conbuildmat.2010.07.020

Publisher's Note Springer Nature remains neutral with regard to jurisdictional claims in published maps and institutional affiliations.